



Comparison of Fokker-Planck and CFD simulations of the RFZ-ST2 upper stage

Leo Basov¹, Moritz Ertl², Tamas Bykerk³

Abstract

We simulate the generic upper stage RFZ-ST2 model with both computational fluid dynamics (CFD) and Fokker-Planck (FP) methods. We use the well established DLR TAU code for the CFD simulations and an in-house FP extension to the Direct Simulation Monte-Carlo (DSMC) code SPARTA. The simulations are done close to the continuum limit. The goal is to validate the models used in the FP implementation versus the well established CFD code and to investigate the limitation of the CFD towards higher Knudsen numbers. To this end, we compare the resulting flow fields and surface distributions of pressure coefficients and heat fluxes between both models. The results agree very well between the models in and around the bow shock. Regions further down stream on the model, especially in areas of strong narrowing in the cross section of the rocket show deviations in the flow field and in the calculated surface heat flux and pressure coefficient. In these regions we expect the computationally more expensive FP model to provide results of higher accuracy. We show that areas of disagreement can be identified using a local Kn number criterion which can be evaluated in post processing from CFD data and used to estimate the quality and validity of the solution. We also use this work to introduce the RFZ-ST2 model, an open source model of a generic upper stage to the high speed aerothermodynamics community.

Keywords: *CFD, Fokker-Planck, upper stage, RFZ-Model*

1. Introduction

Simulations of the flow around a vehicle play an important role in the development of many space applications. The prediction of aerodynamic and aerothermal loads is a relevant feature in the design process. Computational fluid dynamics (CFD) is well established and well suited for applications in denser atmospheres, such as airplanes, first stages or reusable vertical takeoff, vertical landing (VTVL) stages [1]. However, the underlying continuum assumption loses its validity in flow conditions with very low gas density and high level of non-equilibrium. Such flows are characterized by high Knudsen numbers. Several space applications, such as upper stages, space debris or capsules experience flight conditions in these regimes. As we at DLR want to be able to simulate the entirety of space transport missions, we are currently expanding our simulation capabilities on this topic.

In the regimes with higher Knudsen numbers, the flow phenomena are governed by the Boltzmann equation. A common approach to numerically solve it is the Direct Simulation Monte-Carlo (DSMC) method pioneered by Bird [2]. The method is very efficient for high Knudsen numbers but becomes increasingly computationally expensive when approaching the continuum limit. In this regime the Boltzmann equation can be numerically solved using the kinetic Fokker-Planck (FP) method [3]. Similar to DSMC, the FP method relies on simulated particles to transport mass, momentum and energy through the flow domain, but does not resolve individual collisions, which makes it more efficient as the collision frequency increases with lower Kn numbers. At DLR a FP method has been implemented as an extension to the DSMC code SPARTA [4] developed at Sandia National Lab. The method has been extended to model internal degrees of freedom using the Master Equation Ansatz for diatomic [5] and polyatomic molecules [6] as well as mixtures [7]. A gas phase chemistry model is under development [8]. In order to validate the new FP implementations, to better understand the limits of CFD and FP and to investigate the differences, our team is currently looking into several test cases.

¹DLR - Deutsches Zentrum für Luft- und Raumfahrt, AS-RFZ, Göttingen, leo.basov@dlr.de

²DLR - Deutsches Zentrum für Luft- und Raumfahrt, AS-RFZ, Göttingen, moritz.ertl@dlr.de

³DLR - Deutsches Zentrum für Luft- und Raumfahrt, AS-RFZ, Göttingen, tamas.bykerk@dlr.de

The second stage of the RFZ model was selected for the benchmarking studies. The RFZ model is an initiative of the spacecraft department (Institute of Aerodynamics and Flow Technology) at the German Aerospace Center in Göttingen, and aims to provide an open source, common research model for reusable launch vehicles [9]. For comparative numerical studies we provide a consistent geometry for a realistic two-stage rocket with a reusable first stage. The model also includes all necessary boundary conditions and engine parameters. The specifics of the upper stage are presented in ref [10] and can be downloaded via the link provided in ref [11].

In this work we shortly introduce the underlying simulation methods and explain the relevant differences. We provide information on the numerical setups and choice of boundary conditions. We then compare the resulting flow fields and pressure as well as heat flux distributions and discuss relevant differences.

2. Fundamentals

2.1. CFD

The CFD simulations are done using the well established DLR TAU code [12] with the spacecraft extensions [13]. The TAU code is a second order finite volume solver for sets of conservation equations, in our case the compressible laminar Navier-Stokes equations, on hybrid structured-unstructured meshes. The meshes are vertex centered with an edge based dual grid. We simulate with second order spatial accuracy by using the AUSMDV upwinding scheme with a carbuncle fix [14] combined with least squares gradient reconstruction and second order temporal accuracy with a 3-stage explicit Runge-Kutta scheme.

The thermodynamic and transport properties are modeled according to Bottin et al. [15]. The vibrational non-equilibrium and relaxation times are calculated with the model of Millikan and White[16]. The Sutherland Law is used for calculation of viscosity [17]. It is defined as

$$\mu = \mu_0 \frac{T_0 + C}{T + C} \left(\frac{T}{T_0} \right)^{3/2} \quad (1)$$

with μ_0 and T_0 being the reference viscosity and reference temperature respectively and C being the model parameter.

2.2. Kinetic Fokker-Planck

Kinetic models solve the Boltzmann equation which describes the evolution of a scalar distribution function f in flows in a wide range range of regimes:

$$\frac{Df}{Dt} = S_{\text{Boltz}} , \quad (2)$$

where t is time and S_{Boltz} is the Boltzmann collision integral. A common approach to numerically solve Eq. (2) is the DSMC method proposed by Bird [2] which is a stochastic model that solves the spatial and temporal evolution of simulation particles, each of which represents a large number of real molecules. A major assumption behind the model is that due to correct spatial and temporal resolution of the simulation, the evolution of the particles can be split up into a collision step and a free flight step. The interactions between particles are assumed to be binary collisions with instantaneous changes of velocity. These assumptions require grouping of particles in cells with a size in the order of the mean free path and time steps in the order of the collision frequency. The DSMC method has become very mature over the last decades and was shown to be applicable for complex problems with thermal and chemical non-equilibrium. However, applying the model in a flow regime close to continuum makes it prohibitively expensive due the aforementioned resolution criteria (see [18, 19] and references therein).

One approach to make the integro-differential Eq. (2) more manageable is to approximate S_{Boltz} by a Fokker-Planck collision operator S_{FP} :

$$S_{\text{Boltz}} \approx S_{\text{FP}} = - \frac{\partial}{\partial V_i} (A_i f) + \frac{\partial^2}{\partial V_j \partial V_i} \left(\frac{D^2}{2} f \right) , \quad (3)$$

where V is the molecule velocity with indices given in the Einstein notation. Eq. (3) can be solved using a particle method similar to the DSMC approach where the collision step is replaced by a velocity update of the particles which does not rely on the building of collision pairs making the computational cost of the FP method become independent of the Kn number. The drift coefficient A_i and the diffusion coefficient D of Eq. (3) are model parameters chosen in such a way that production terms calculated using the Boltzmann collision operator are reproduced by the production terms using the FP collision operator [20]

$$P_{\text{Boltz}} \stackrel{!}{=} P_{\text{FP}}. \quad (4)$$

For the simulations presented in this paper we use the FP cubic model [3]. In this approach a cubic polynomial ansatz is made for the drift coefficient. The coefficients of the polynomial are fitted by calculating the set of production terms defined as

$$P(X) = \int S X dC, \quad (5)$$

$$X \in \{C_i, C_i C_j, C_{<i} C_{j>} C_i C_j C_j\} \quad (6)$$

where $C = V - U$ is the thermal molecule velocity and U the macroscopic gas velocity. Here $C_{<i} C_{j>}$ refers to the deviatoric part of the tensor $C_i C_j$. Equality of production terms of the same order between two kinetic models shows that these models display equal behaviour in the continuum limit [21]. Therefore, choosing this set ensures that velocity moments up to the heat flux are correctly reproduced by FP model.

For the relaxation of internal degrees of freedom we use the master equation extension for the FP model [5]. Variable collision numbers defined according to Bird [2] are used for the calculation of the rotational and vibrational relaxation times to match the Millikan-White model used in TAU. For the FP relaxation time defined as $\tau = 2\mu/p$ the Sutherland viscosity model is used.

2.3. Non-Equilibrium Considerations

According to Gallis et al. [22] the level of non-equilibrium in a system can be assessed using so called *system* and *local* Kn numbers. The former is defined by the ratio between the mean free path and a characteristic system length and estimates the ratio between inter particle and particle-wall collisions. The later is the ratio between the mean free path and a *hydrodynamic length scale* and can be used as a measure for local deviations from equilibrium assumptions.

Non-equilibrium effects enter the Navier-Stokes equations via the formulations for heat flux and shear stress. Those quantities require a closure which is sensitive to large deviations from the Maxwell distribution function. The heat flux and shear stress can be expressed given the constitutive equations:

$$\mathbf{q} = -k\nabla T \quad (7)$$

$$\tau = \mu \left\{ \left(\nabla \mathbf{U} + \nabla \mathbf{U}^T \right) - \frac{2}{3} (\nabla \cdot \mathbf{U}) \mathbf{I} \right\} \quad (8)$$

where \mathbf{U} is the velocity vector, k is the thermal conductivity, μ the dynamic viscosity, and \mathbf{I} is the unit matrix. The terms can be made dimensionless as

$$\tilde{\mathbf{q}} = \frac{1}{\rho c_m^3} \mathbf{q} \quad (9)$$

$$\tilde{\tau} = \frac{1}{\rho c_m^2} \tau \quad (10)$$

where ρ the is the density and $c_m = \sqrt{2k_B T/m}$ the most probable speed.

The local heat flux and shear stress Kn number are thus defined as

$$\text{Kn}_q = |\tilde{\mathbf{q}}| = \frac{|\mathbf{q}|}{\rho c_m^3} \quad (11)$$

$$\text{Kn}_\tau = |\tilde{\tau}| = \frac{|\tau|}{\rho c_m^2}. \quad (12)$$

These Kn numbers can be seen as indicators of the applicability of Fourier's and Newton's laws in terms of heat conductivity and shear stress.

As the investigated flows are likely to have regions of flow rarefaction with departure from equilibrium we want to investigate whether these local Kn numbers can be used to reliably predict these areas from CFD simulation results. In this way we could identify cases in which CFD methods lose their validity and switch to a kinetic approach.

3. Numerical Setups and Geometry

We use three simulations of increasing complexity to investigate our research questions:

1. An unsteady 0D reactor with high temperature
2. A 2D cylinder in a steady state $Ma = 10$ flow
3. The RFZ upper stage as a 2D model at the trajectory point for $h = 67.35$ km

All three setups use a common set of settings and parameters, which are described in this section, while the geometries and parameters specific to each setup are provided in separate chapters, below. All simulations are done using diatomic nitrogen, with the species properties provided in table 1, and the FP method specific parameter given in table 2.

Table 1. Species

| Molecule | m / kg | dof_{rot} | dof_{vib} | $\theta_{\text{vib}} / \text{K}$ | $\theta_{\text{rot}} / \text{K}$ |
|----------|------------------------|---------------------------|---------------------------|----------------------------------|----------------------------------|
| N_2 | 4.65×10^{-26} | 2 | 2 | 3393.48 | 2.875 |

Table 2. FP Parameters

| $d_{\text{ref}} / \text{m}$ | $T_{\text{ref}} / \text{K}$ | ω | Z_{rot}^{∞} | T^* / K | C_1 / K | $C_2 / \text{K}^{1/3}$ |
|-----------------------------|-----------------------------|----------|---------------------------|------------------|------------------|------------------------|
| 4.07×10^{-10} | 273.15 | 0.74 | 18.1 | 91.5 | 9.1 | 220 |

The Millikan-White model is used to calculate the relaxation with the parameters given in table 3. The

Table 3. CFD Millikan-White Parameters

$$\frac{a}{221.493\,526} \quad \frac{b}{0.028\,898}$$

viscosity modelling is done using the Sutherland Law with the parameters given in table 4. The application of this model to FP has been described in more detail in section 2.2.

Table 4. Sutherland Viscosity Parameters for both CFD and FP

| μ_0 / Pas | T_0 / K | C / K |
|------------------------|------------------|----------------|
| 17.81×10^{-6} | 300.55 | 111 |

3.1. 0D Reactor Setup

Both the FP and the CFD models simulate a 0d reactor which is initialized with N_2 at a density of $\rho^0 = 4.65 \times 10^{-3} \text{ kg m}^{-3}$. The rotational temperature is assumed to be equal to the vibrational at the beginning of the simulation with its values being $T_{\text{rot}}^0 = T_{\text{vib}}^0 = 2000 \text{ K}$ and the translational temperature is set to $T^0 = 8000 \text{ K}$. The unsteady simulation is performed for a duration of $t^{\text{end}} = 1.0 \times 10^{-4} \text{ s}$. For the FP simulation we use a single cubic cell with a volume of $1 \times 10^{-12} \text{ m}^3$ with periodic boundary conditions as the simulation domain. The time step is chosen to be $\Delta t = 1.0 \times 10^{-6} \text{ s}$ with the particle weight being

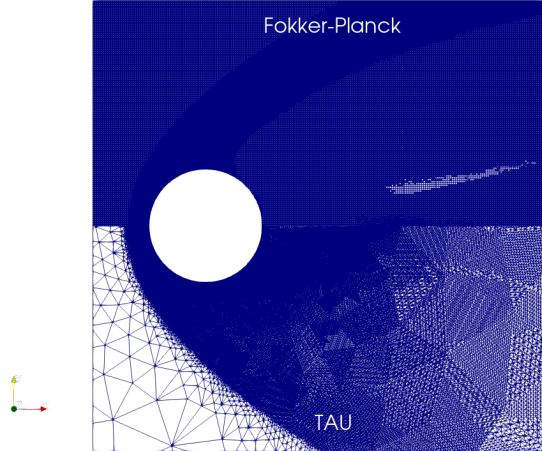


Fig 1. Comparative visualisation of the 2D Cylinder grid resolution.

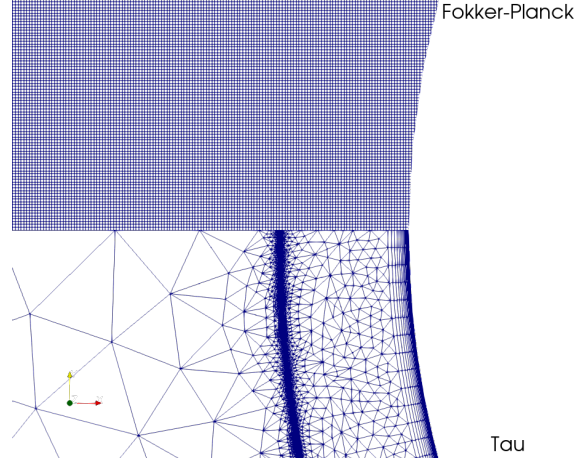


Fig 2. Comparative visualisation of the RFZ-ST2 grid resolution of the nose section.

set to $w = 1 \times 10^5$. The particle weight is the number of real molecules being represented by a single numerical particle used in our FP simulations. For the CFD we use a square box from 4 by 4 by 2 cells as a reactor. A small initial velocity is set to $v^0 = 0.001 \text{ m s}^{-1}$ and the simulation is performed with a time step of $\Delta t = 1.0 \times 10^{-8} \text{ s}$.

3.2. 2D Cylinder Setup

We simulate the steady state hypersonic N_2 flow around a cylinder with a diameter of $D = 0.3 \text{ m}$ aligned with the center of the simulation domain. The inflow conditions are $\rho_\infty = 2.325 \times 10^{-4} \text{ kg m}^{-3}$, $T_\infty = 300 \text{ K}$ and $Ma_\infty = 10$. For the cylinder an isothermal wall with $T_w = 300 \text{ K}$ is assumed. The FP simulations uses a time step of $\Delta t = 1 \times 10^{-6} \text{ s}$, a particle weight of $w = 0.25 \times 10^{15}$, and diffusive scattering at the cylinder wall with an accommodation factor of $\alpha = 1$. The simulation is performed in a box with a side length of $L_{\text{BOX}}^{\text{FP}} = 1.2 \text{ m}$. The simulation grid is adapted such that each cell contains between 10 and 100 simulation particles. For the CFD simulation a square box with edge length of $L_{\text{BOX}}^{\text{TAU}} = 2.0 \text{ m}$ was used. The case is run as a steady state simulation. An initial coarse grid is generated with CENTAUR. The grid is adapted with TAU Adaptation after achieving steady state for five consecutive grid refinement cycles. The final TAU grid as well as the FP simulation grids can be seen in Fig. 1.

3.3. 2D RFZ Upper Stage Setup

3.3.1. Definition of the Rocket Geometry and Simulation Grids

The RFZ-ST2 model is a generic model of an upper stage for a VTVL reusable launch vehicle which is shown in Fig. 3. It is part of the RFZ model suite of open source rocket models created to provide a common research geometry for simulating VTVL reusable launch vehicles. The upper stage has a length of $L_{\text{RFZ-ST2}} = 28 \text{ m}$ and a diameter of $D_{\text{RFZ-ST2}} = 3.66 \text{ m}$. The geometry sources are freely available at [11].

Both simulations are exploiting the rotational symmetry of the configuration by reducing the computational domain to a 2D axisymmetric mesh. In the case of CFD, first, a coarse grid is generated using CENTAUR with a farfield radius of $r_{\text{farfield}} = 20 \cdot L_{\text{RFZ-ST2}}$ and with 20 prism layers at the walls with a dimensionless first layer thickness of $y^+ < 1.0$. Then the mesh refinement functionality of TAU, TAU Adaptation, is used to obtain a well resolved grid for the relevant flow structures, such as the shocks and the shear layers. The final CFD mesh used in this work consists of over 6 million grid points. The resolution of the CFD is higher than necessary in most regions, but was chosen to more closely match the grid resolution of the FP setup. At this resolution the solver had to be switched from steady state to quasi steady state using dual time stepping in order to obtain a converged resolution, due to the high

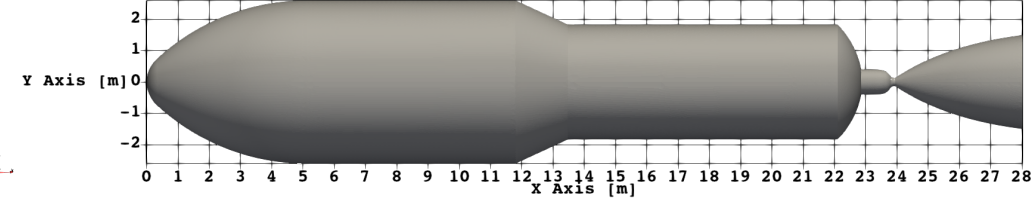


Fig 3. Visualisation of the RFZ-ST2 upper stage geometry.

differences in local CFL numbers. Therefore, no further refinement was done after this step.

For the FP simulation domain we used a rectangular plane with dimensions $L_x = 41\text{ m}$ and $L_y = 12\text{ m}$ in x and y direction respectively. The initial simulation grid was generated containing 410×120 cells. It was then locally adapted during a pre-run using SPARTA's build in grid adaptation method until each cell contained between 10 and 100 numerical particles. The final simulation grid consists of over 21 million cells. The mesh representing the surface of the rocket was generated with FreeCAD using its *PointsFromMesh* feature and contains 3192 elements. A visualisation of the structure of both meshes for the nose section is shown in Fig. 2

3.3.2. Settings and Boundary Conditions

A trajectory point within the applicable region of the CFD method is selected from [11] to be at an altitude of $h = 67.35\text{ km}$. At this point the simulated second stage of the vehicle is assumed to be in a short free flight phase with it's main engine not yet ignited. The trajectory point is used to define the farfield boundary condition for both simulations with a velocity in x -direction $v_\infty = 2249.72\text{ m s}^{-1}$, a density $\rho_\infty = 1.20 \times 10^{-4}\text{ kg m}^{-3}$ and a temperature $T_\infty = 226.9\text{ K}$. The resulting Mach number is, therefore, $Ma = 7.327$, which differs slightly from the reference, due to the choice of N_2 instead of air.

A Knudsen number of $\text{Kn} = 1.3 \times 10^{-4}$ was calculated for this flight regime using the largest diameter of the rocket as the reference length with the mean free path being calculated using the VHS model with parameters taken from [2]. For the CFD the boundary condition for surfaces of the upper stage are set as viscous walls with the laminar subtype and an isothermal wall temperature $T_w = 300\text{ K}$. The FP simulation uses a diffuse boundary condition for the surface with an accommodation coefficient of $\alpha = 1$ and a constant wall temperature of $T_w = 300\text{ K}$. For the FP simulation a time step of $\Delta t = 1 \times 10^{-6}\text{ s}$ was used with a particle weight of $w = 5 \times 10^{18}$. The simulation was performed for 20 000 steps to reach steady state. After reaching steady state the final results were averaged over 10 000 steps.

4. Results

4.1. 0D Reactor

The 0D reactor case is used to evaluate and compare the temporal development of the non-equilibrium temperatures. For the CFD simulation both the translational temperature T and the vibrational temperature T_{vib} are spatially averaged over all cells of the reactor for each time step. The comparison between translational and vibrational relaxation is plotted in Fig. 4.

A very good agreement in both the temporal relaxation and in the reached equilibrium temperatures between FP and the CFD is observed. This confirms that non-equilibrium modelling with parameters for the Millikan-White relaxation model are well chosen even though the model formulation slightly differs for the two methods.

4.2. 2D Cylinder

The 2D cylinder case is used to validate and compare the spatial behaviour of the numerical modelling. The visualisations of the relevant steady state field values: translational temperature T , vibrational temperature T_{vib} , velocity magnitude $|\vec{v}|$ and density ρ are shown in Fig. 5. The direction of the flow is from left to right.

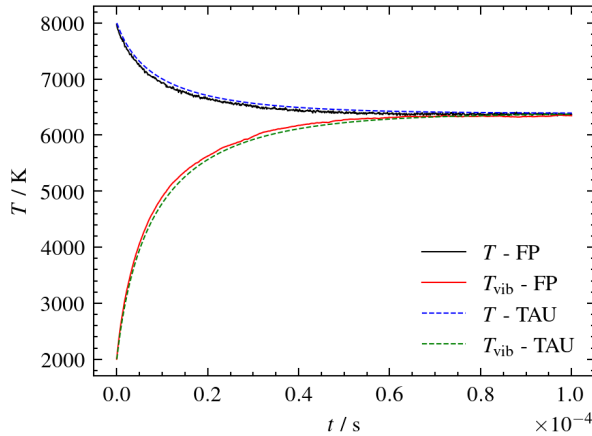


Fig 4. 0D simulation of translational-vibrational temperature relaxation.

The plots show, that the general flow structure is well captured both by CFD and by FP. Shock off set and shock angle compare very well as do the distributions of temperature, velocity and density in front of the cylinder. The temperature boundary is a bit wider and more smeared out in the FP. This is due to the lower mesh resolution at the wall - a result of the structured mesh limitation. The distribution of vibrational temperature upstream of the cylinder is slightly shifted, with the FP displaying a wider region of high T_{vib} and the upstream distribution being shifted stream-wards by this offset.

The distribution of the temperature T and the vibrational temperature T_{vib} along a center line upstream of the cylinder is provided in Fig. 6. Observing the temperature profiles it is clear that both models are in good agreement in capturing the position of the shock seen as a steep increase in the translational temperature T . The differences between the profiles is seen in the relaxation region of the vibrational temperature where T_{vib} relaxes faster in the FP compared to the CFD case. This behavior is also expressed in the 2D plot in Fig. 5b where the higher relaxation rate presents itself in a higher thickness of the high vibrational temperature region in the FP compared to the CFD. The computational grid is ruled out as a cause for this thicker region, since the same behaviour can not be observed in the other plots. To better understand the differences in the simulation results between FP and TAU an analytical comparison between the vibrational relaxation model is performed in Appendix A. Plotting the fraction between vibrational relaxation time as calculated in FP τ^{FP} over the vibrational relaxation time as calculated in CFD using the Millikan-White model τ^{MW} using Eqn. (19) we can see that the relaxation time is smaller for FP especially for smaller temperatures using the data provided in the literature (see Fig. 7). This behaviour is less prominent in the 0D as seen in Fig. 4 case most likely due to the higher temperatures used in the test case as the the relaxation times converged towards one another for large temperatures. We expect to be able to provide even better results in the future by using coefficients better fitted to accommodate both methods.

The main differences in the flow field can be observed in the wake of the cylinder. This is the region were we expect the flow state to deviate from the continuum assumptions. Even though the validity region of both the FP and the CFD model lies close to equilibrium, the FP model is expected to predict the heat fluxes more accurately as the model coefficients are chosen in such a way as to correctly reproduce the production term for this order of velocity moments as described in section 2.2. Therefore the FP is expected to provide more accurate results in regions of non-equilibrium.

For further analysis we use the local Kn numbers defined in Eqn. (11) and Eqn. (12). For the calculation of the cell local heat flux q , as given in Eqn. (9), the thermal conductivity is set to a constant value of $k = 0.025 \text{ W m}^{-1} \text{ K}^{-1}$. Sutherland's viscosity law is assumed in the shear stress calculation. The results can be seen in Fig. 8a and 8b respectively. If we calculate the maximum value of both parameters $\text{Kn}_{\max} = \max(\text{Kn}_q, \text{Kn}_\tau)$ for each cell, as seen in Fig. 8c we get a good prediction of areas with non-

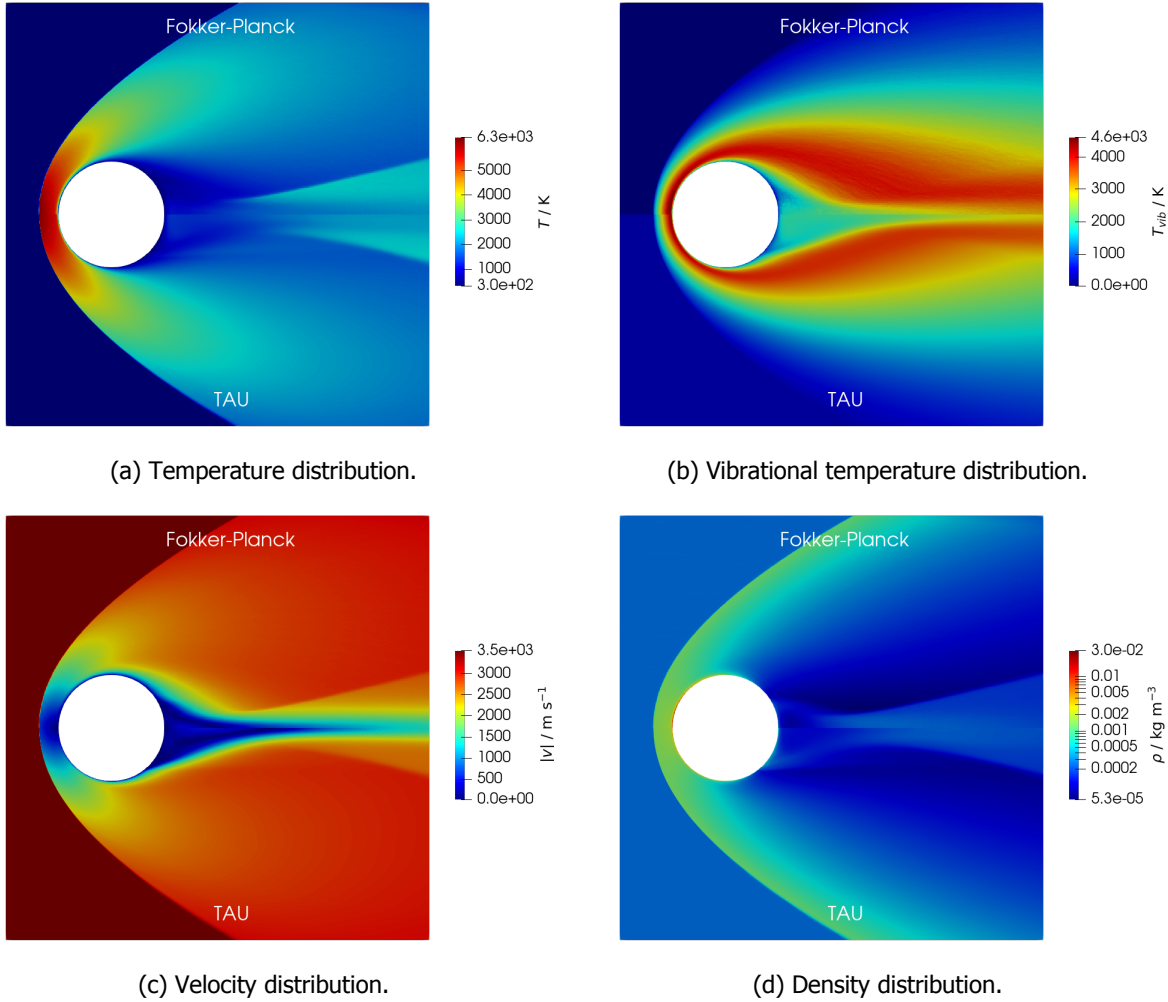


Fig 5. Visualisations for the 2D cylinder flow case.

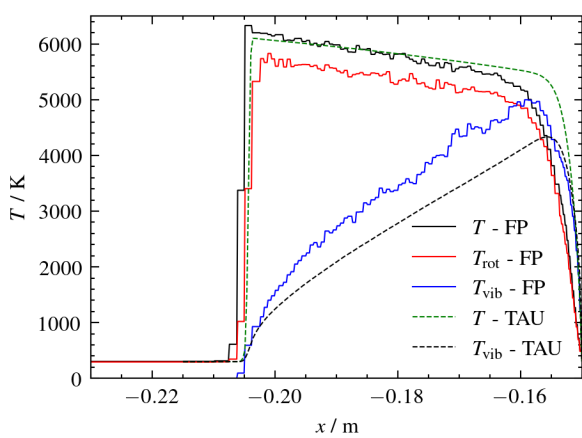


Fig 6. Temperature relaxation over the shock of the 2D cylinder flow.

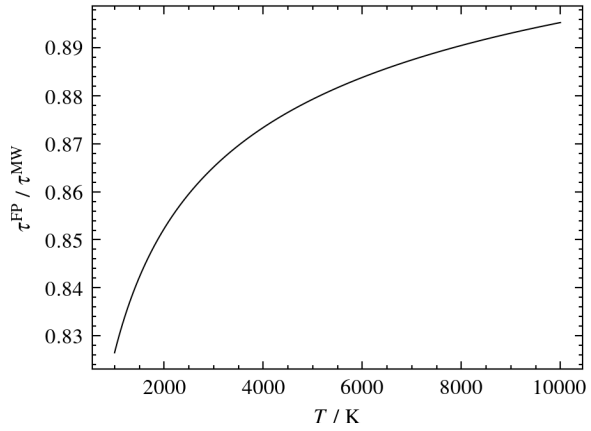


Fig 7. Comparison between the vibrational relaxation times as calculated in FP and CFD using the Millikan-White model.

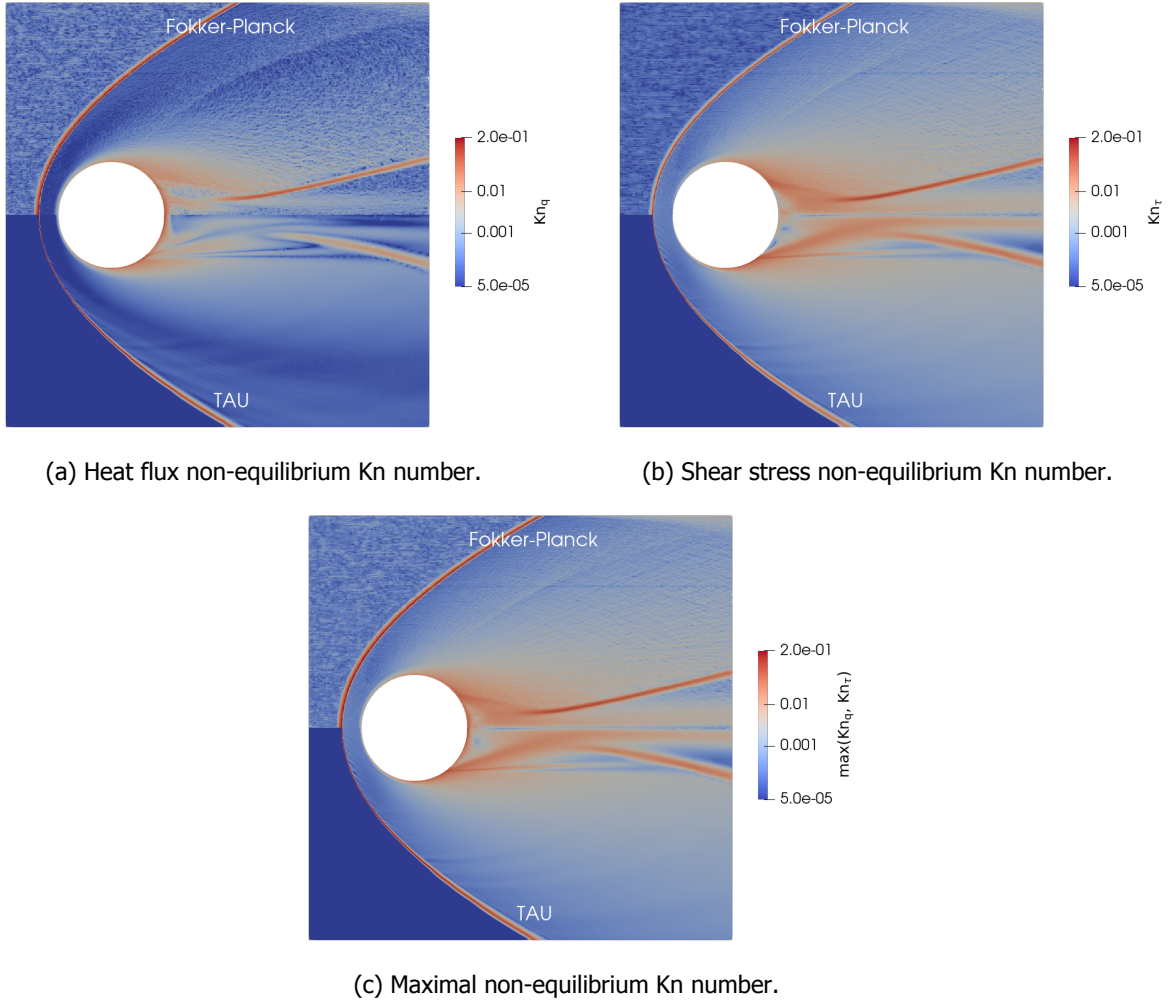
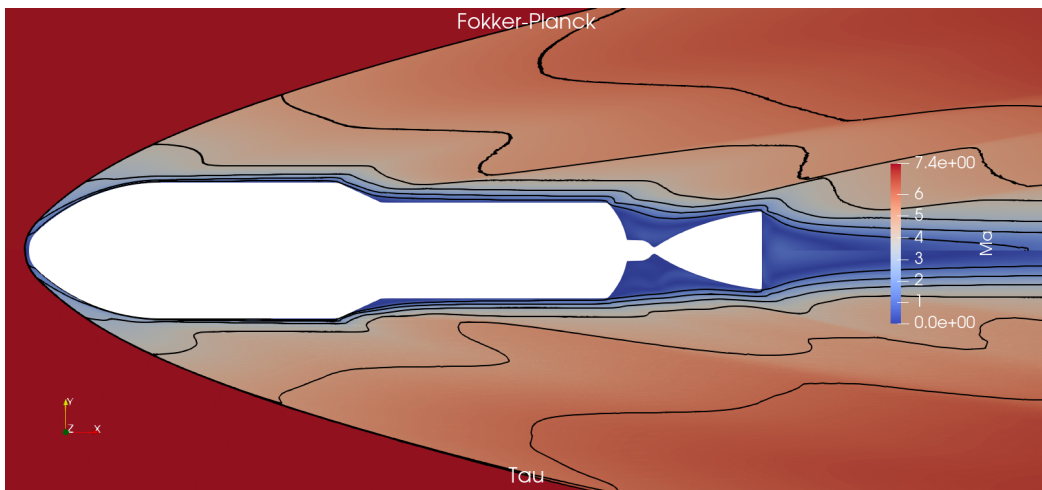


Fig 8. Non-equilibrium parameters.

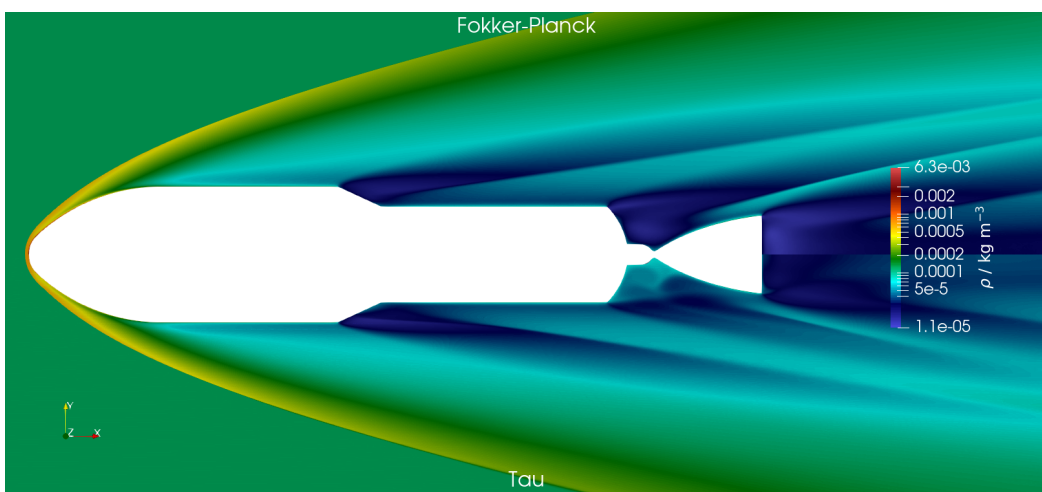
equilibrium effects. The predicted regions in the wake of the cylinder match well with the areas in which large discrepancies between the FP and the TAU simulations can be observed. Using this criteria we can identify areas in which we predict FP to produce more accurate results than CFD. Additionally, while the quantitative results differ slightly, the qualitative identification of relevant regions is clearly possible. Therefore, a prediction of regions with lower CFD fidelity seems possible already from CFD results alone.

4.3. RFZ Upper Stage

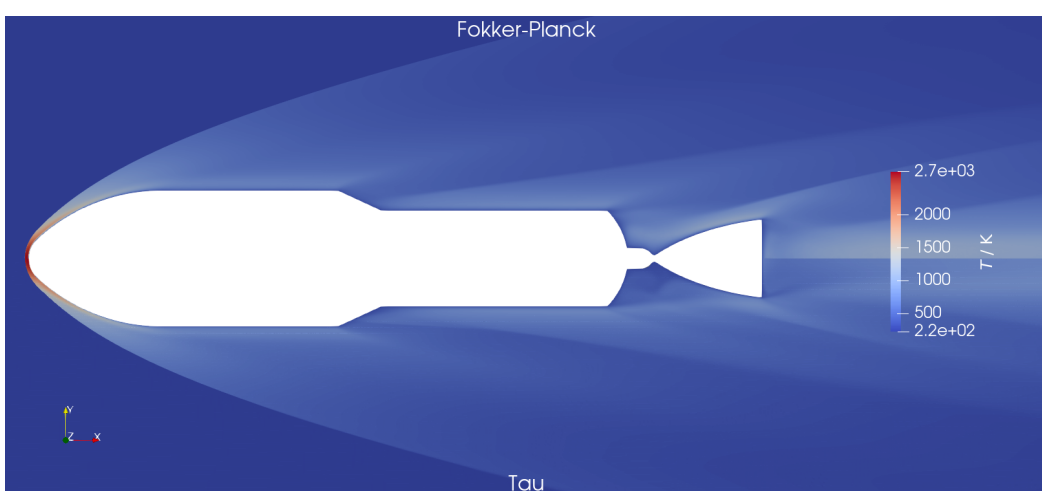
The results of the comparison simulations between FP and TAU are visualized in Fig. 9. The comparison shows a general good agreement of the flow field. The Mach number in particular as seen in Fig. 9a enhanced by a Mach contour plot agrees very well between the two models. Especially in high density areas such as behind the shock at the nose cone we can see that the contour lines of the Mach number meet at the mirror plane between the two plots as seen in Fig. 10. Some differences in the contour lines are visible close to the vehicle surface. These are due to the difference in grid resolutions, with the the CFD having a much finer dedicated boundary layer mesh. Additionally, one can observe that the shock stand off distance is somewhat higher in the FP simulation due to the difficulty of achieving the very high resolution needed. FP uses simulation particles with each particle representing a large number of real molecules. As the cells become smaller and smaller more and more particles are needed



(a) Mach number distribution with contour lines.



(b) Density distribution.



(c) Temperature distribution.

Fig 9. Comparative visualisation of the RFZ-ST2 upper equilibrium simulation.

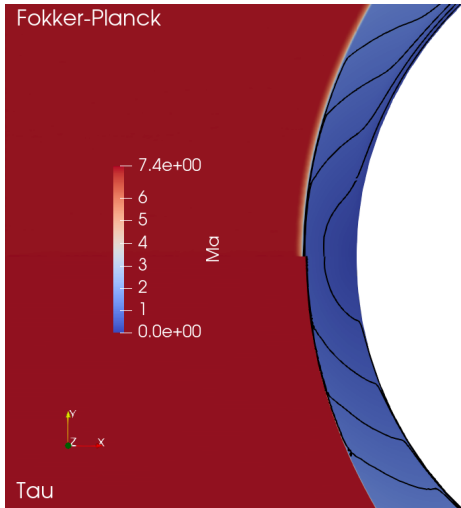


Fig 10. Comparative visualisation of the RFZ-ST2 upper equilibrium simulation for Mach number distribution - close up.

throughout the simulation domain to fill up all cells with a sufficient number of particles. This leads to difficulties resolving small flow structures for large scale simulations as in the given case. This also results in a slightly larger shock width resulting in a higher temperature behind the shock in the FP, leading to differences between the two simulations.

Larger differences can be observed in areas of decreasing rocket cross section, where flow separation is likely to occur. On our upper stage these areas are mainly around the base plate and at the transition from the fairing diameter to the rocket diameter. Here we expect a region of strong rarefaction and therefore a large departure from continuum assumptions made for CFD similar to the case of the 2D cylinder flow. Indeed, in the plots for temperature in Fig. 9c and density in Fig. 9b the visible differences are most pronounced in the base plate region and behind the (inactive) nozzle exit, whose geometry in this simulation is defined as a flat wall.

The assumption for the differences can be confirmed by analysing the applied non-equilibrium criteria as discussed in the previous section. Visualised in Fig. 11 is the maximum of the two local non-equilibrium Kn numbers Kn_{\max} . The number is normalized to one for better visualization. Areas of strong deviation between CFD and FP are captured by Kn_{\max} . In addition to the areas behind the base plate and the area behind the fairing is identified, despite no major differences being visible in the Mach number, density and temperature plots.

To further investigate the differences between the simulations we look at the specific surface heat flux q and pressure coefficient C_p which are shown plotted on a logarithmic scale over the length of the rocket in Fig. 12.

The general trends for both surface data are in good agreement. However, in particular for C_p seen in Fig. 12b larger differences between the FP and TAU simulations are visible in the areas around the nozzle throat, behind the nozzle exit and behind the kink of the payload fairing. The comparison of the heat loads in Fig. 12a is good, especially in frontal region until the end of the fairing. A difference is the predicted maximum heat flux in the stagnation point of the nose, which might be related to the resolution based temperature differences behind the shock, which are described in the first part of this section. For the other differences, however, a similar behaviour to the C_p plot is visible in the heat flux distribution with the locations of highest differences mapping to the predicted locations in Fig. 11. It is noticeable, that the regions identified by the Kn_{\max} criterion, but which were not obviously identifiable from the flow field are now clearly relevant in the surface data analysis.

All areas captured by Kn_{\max} identified relevant differences in our comparison, showing that the criterion

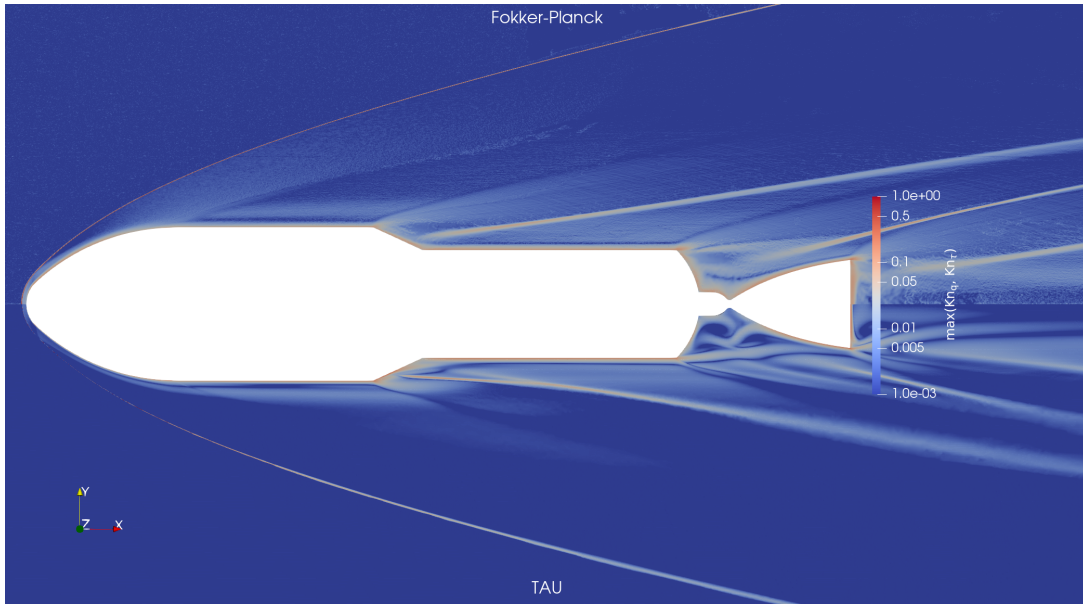


Fig 11. Comparative visualisation of the RFZ-ST2 upper equilibrium simulation for $\max(\text{Kn}_q, \text{Kn}_\tau)$.

can be used as a basis to asses the accuracy of CFD simulations. In situations where a high accuracy in identified regions is necessary we expect FP to produce higher quality results.

5. Conclusion and Outlook

We compared simulations of supersonic flow near the continuum limit with classical CFD, using the DLR TAU code, and the Fokker Planck particle method, using an in-house FP implementation in SPARTA. We validated our modelling assumptions using a 0D reactor case and a simple 2D cylinder geometry. We investigated the applicability of our methods to our main bench-marking case, a generic upper stage. The initial results show, that this case is a good choice for our research. It is a good representation of the real applications we want to investigate in the future it provides regions showing strong rarefaction effects caused by steep variations in cross section of the geometry. We also hope that the open source nature of the RFZ project inspires other researchers to use it for comparative studies and share data which would benefit the community.

The general flow features compare well between the FP and the CFD in all cases. The position and shape of shocks as well as the distributions of temperature and density are in good agreement. Some discrepancies exist, pointing out the different strength and weaknesses of the methods. In the CFD the flow prediction is less accurate in regions, where the density is low and flow separation is possible. We show that non-equilibrium parameters can be used to identify areas where the CFD model starts to lose its validity and can help to decide, if and when a switch to a kinetic model, like FP, might be necessary to achieve better results. The non-equilibrium parameters, in our cases, are identifying the same regions for FP and CFD. Therefore, using CFD data, even in rarefied regions, to predict the applicability of the methods seems to be possible.

The work in this paper is a step towards providing aerothermal simulation capabilities for a wide range of space applications and missions. We strive to improve our modelling and to establish best practices for working with both methods. As a next step, we already started on enhancing the upper stage simulation to model poly-atomic mixtures of several species in order to correctly represent the air atmosphere. After that we will investigate chemistry modelling for post combustion and possible dissociation effects.

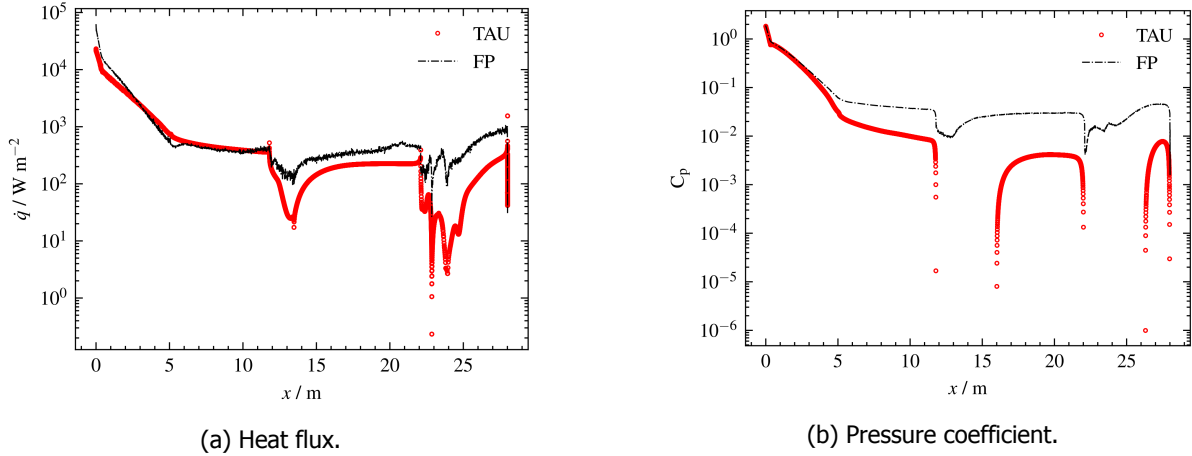


Fig 12. Comparative visualisation of the RFZ-ST2 upper equilibrium simulation of surface values plotted over length of the rocket.

6. Acknowledgements

The authors would like to thank Georgii Oblapenko, Mariasole Laureti and Sebastian Karl for fruitful discussions on the topic.

A. Comparison Between FP and Millikan-White Vibrational Relaxation Times

To better understand the differences in the simulation results between FP and TAU we provide an analytical comparison between the vibrational relaxation models. The TAU code uses the model of Millikan and White in the form

$$p\tau^{\text{MW}} = \exp\left(a(T^{-1/3}-b)-6.894\right) = \underbrace{\exp(-ab - 6.894)}_{\tilde{b}} \exp\left(aT^{-1/3}\right) \quad (13)$$

with a and b being model parameters. Our FP uses the Landau-Teller model [23] for the relaxation of the internal energy modes

$$\frac{\partial e_{\text{int}}}{\partial t} = \frac{e^{\text{eq}} - e_{\text{int}}}{\tau^{\text{FP}}}. \quad (14)$$

Here e_{int} is the energy of the internal energy mode, e^{eq} the equilibrium energy, and τ^{FP} the relaxation time in the form

$$\tau_{\text{vib}}^{\text{FP}} = \frac{Z_{\text{vib}}}{\nu_{\text{coll}}} \quad (15)$$

with ν_{coll} being the collision frequency and Z_{vib} the so called collision number representing the average number of particle collisions required for the internal energy mode to reach equilibrium with the translational energy. For the collision number we use a formulation proposed by Bird [2]

$$Z_{\text{vib}} = \frac{C_1}{T^\omega} \exp\left(\frac{C_2}{T^{1/3}}\right) \quad (16)$$

together with the VHS model [2] for the calculation of the collision frequency

$$\nu_{\text{coll}} = 4d_{\text{ref}}^2 n \sqrt{\frac{\pi k_B T_{\text{ref}}}{m}} \left(\frac{T}{T_{\text{ref}}}\right)^{1-\omega}. \quad (17)$$

If we assume ideal gas with $p = k_B n T$ we can cast the vibrational relaxation time for the FP model in form comparable with Millikan-White model used in TAU

$$p\tau^{\text{FP}} = nk_B T \frac{Z_{\text{vib}}}{\nu_{\text{coll}}} = \underbrace{\frac{C_1}{4d_{\text{ref}}^2 T_{\text{ref}}^{\omega-1/2}} \sqrt{\frac{k_B m}{\pi}}}_{\tilde{C}_1} \exp\left(C_2 T^{-1/3}\right). \quad (18)$$

Using Eqn. (13) and Eqn. (18) we can write for the fraction of the vibrational relaxation times of the two used models:

$$\frac{\tau^{\text{FP}}}{\tau^{\text{MW}}} = \frac{\tilde{C}_1}{\tilde{b}} \exp\left((C_2 - a)T^{-1/3}\right). \quad (19)$$

Given the data used for N₂ in Tab. 1, 2, and 3 we can calculate the reference model parameters \tilde{b} and \tilde{C}_1 to

$$\tilde{b} = 1.68336 \times 10^{-6} \quad (20)$$

$$\tilde{C}_1 = C_1 \times 1.77504 \times 10^{-7} = 1.61529 \times 10^{-6}. \quad (21)$$

References

- [1] Moritz Ertl, Tobias Ecker, Joseph Klevanski, Sven Krummen, and Etienne Dumont. Aerothermal analysis of plume interaction with deployed landing legs of the callisto vehicle. In *9th European Conference for Aeronautics and Space Sciences*, 2022.
- [2] G. A. Bird. *Molecular Gas Dynamics and the direct Simulation of Gas Flows*. Oxford University Press, New York, 1994.
- [3] M. H. Gorji, M. Torrilhon, and P. Jenny. Fokker–Planck model for computational studies of monatomic rarefied gas flows. *Journal of Fluid Mechanics*, 680:574–601, August 2011.
- [4] S. J. Plimpton, S. G. Moore, A. Borner, A. K. Stagg, T. P. Koehler, J. R. Torczynski, and M. A. Gallis. Direct simulation Monte Carlo on petaflop supercomputers and beyond. *Physics of Fluids*, 31(8):086101, August 2019.
- [5] Christian Hepp, Martin Grabe, and Klaus Hannemann. Master equation approach for modeling diatomic gas flows with a kinetic Fokker-Planck algorithm. *Journal of Computational Physics*, 418:109638, October 2020.
- [6] Leo Basov and Martn Grabe. Modeling of Polyatomic Gases in the Kinetic Fokker-Planck Method by Extension of the Master Equation Ansatz. In *32ND INTERNATIONAL SYMPOSIUM ON RAREFIED GAS DYNAMICS: RGD32*, Seoul, KOR, 2022. Accepted Manuscript.
- [7] Christian Hepp, Martin Grabe, and Klaus Hannemann. A kinetic Fokker–Planck approach for modeling variable hard-sphere gas mixtures. *AIP Advances*, 10(8):085219, August 2020.
- [8] Leo Basov and Martin Grabe. Modeling of Chemical Reactions in Rarefied Gas Flows by the Fokker-Planck Method. SIAM Conference on Computational Science and Engineering (CSE23), 2023.
- [9] Tamas Bykerk. A standard model for the investigation of aerodynamic and aerothermal loads on a re-usable launch vehicle. In *Aerospace Europe Conference 2023 - 10th EUCASS - 9th CEAS, Lausanne, Switzerland*, 2023.
- [10] Tamas Bykerk. A standard model for the investigation of aerodynamic and aerothermal loads on a re-usable launch vehicle - second stage geometry. In *HiSST: International Conference on High-Speed Vehicle Science & Technology, 14–19 April 2024, Busan, Korea*, 2024.
- [11] Tamas Bykerk. The rfz model - a standard model for the investigation of aerodynamic and aerothermal loads on a re-usable launch vehicle. <https://zenodo.org/communities/rfz-model>. Accessed: 2023-09-16.
- [12] D. Schwamborn, T. Gerhold, and R. Heinrich. The dlr tau-code: recent applications in research and industry. In *ECCOMAS CFD 2006 CONFERENCE*, 2006.
- [13] Klaus Hanemann, Jan M. Schramm, Alexander Wagner, Sebastian Karl, and Volker Hanemann. A closely coupled experimental and numerical approach for hypersonic and high enthalpy flow investigations utilising the heg shock tunnel and the dlr tau code. Technical report, DLR, 2010.

- [14] Yasuhiro Wada and Meng-Sing Liou. A flux splitting scheme with high-resolution and robustness for discontinuities. In *32nd Aerospace Sciences Meeting and Exhibit*, 1994.
- [15] B. Bottin. *Aerothermodynamic model of an Inductively-Coupled Plasma Wind Tunnel*. Phd thesis, Von Karman Institute for Fluid Dynamics., 1999.
- [16] R. C. Millikan and D. R. White. Systematics of vibrstional relaxation. *Journal of Chemical Physics*, 39(12):3209–3213, 1963.
- [17] William Sutherland. LII. *The viscosity of gases and molecular force*. 36(223):507–531.
- [18] G.A. Bird. Recent advances and current challenges for DSMC. *Computers & Mathematics with Applications*, 35(1-2):1–14, January 1998.
- [19] M. S. Ivanov. Current Status and Prospects of the DSMC Modeling of Near-Continuum Flows of Non-Reacting and Reacting Gases. In *AIP Conference Proceedings*, volume 663, pages 339–348, Whistler, British Columia (Canada), 2003. AIP. ISSN: 0094243X.
- [20] Patrick Jenny, Manuel Torrilhon, and Stefan Heinz. A solution algorithm for the fluid dynamic equations based on a stochastic model for molecular motion. *Journal of Computational Physics*, 229(4):1077–1098, February 2010.
- [21] Henning Struchtrup. *Macroscopic transport equations for rarefied gas flows*, pages 145–160. Springer Berlin Heidelberg. Series Title: Interaction of Mechanics and Mathematics.
- [22] M. A. Gallis, J. R. Torczynski, D. J. Rader, M. Tij, and A. Santos. Normal solutions of the boltzmann equation for highly nonequilibrium fourier flow and couette flow. 18(1):017104.
- [23] L.D. Landau and E. Teller. On the Theory of Sound Dispersion. In *Collected Papers of L.D. Landau*, pages 147–153. Elsevier.